Chemistry–A European Journal

Research Article
doi.org/10.1002/chem.202402084

Chemistry Europe
European Chemical Societies Publishing

www.chemeurj.org

Thermochemistry of Solid-State Formation, Structure, Optical, and Luminescent Properties of Complex Oxides Eu_2MeO_6 (Me–Mo, W), $Eu_2W_2O_9$: A Combined Experimental and DFT Study

Yulia V. Seredina,[a] Aleksandr S. Oreshonkov,[b, c] Maxim S. Molokeev,[d, e] Alexander E. Sedykh,[f] Aleksandr S. Aleksandrovsky,[g, h] Maksim A. Zhernakov,[f, i] Nikolay A. Khritokhin,[a] Nikita O. Azarapin,[a] Polina O. Glukhova,[a] Natalia A. Shelpakova,[a] Klaus Müller-Buschbaum,[f, j] and Yuriy G. Denisenko*[a, f, k]

Complex oxides Eu_2MeO_6 (Me–Mo, W), $Eu_2W_2O_9$ were obtained by a solid-phase reaction between binary oxides. The thermodynamic and kinetic mechanisms of the reaction processes were established using a variety of physical-chemical methods. All compounds obtained in this work crystallize in the low-symmetry monoclinic system, forming complex framework structures, which determine a set of very valuable physical-chemical properties. Comparison of experimental Kubelka-Munk functions and DFT- calculated absorption spectra shows adequate agreement and reveals the origin of the fundamental absorption. In addition, the deficiency in DFT calculations in the part of mutual contribution of CTBs of Mo–O and W–O, from one side, and Eu–O contributions, from the other side, is reported. Calculations of absorption spectra are shown to be superior to band structure analysis in the determination of optical band gaps. Additionally, luminescent properties of Eu_2MeO_6 and $Eu_2W_2O_9$ compounds were investigated. These studies provide a better understanding of the electronic and optical properties of the compounds Eu_2MeO_6 and $Eu_2W_2O_9$, along with their potential applications in various areas.

Introduction

Complex oxides are an attractive material family, as the wide range of crystal structures they exhibit allows for the finding of various properties. Among complex oxides, piezo-[1–3] and thermoelectrics,[4–7] high-temperature superconductors,[8–10] magnetic materials,[11,12] and catalysts[13–15] have been discovered. Nevertheless, the potential applications of complex oxides remain vast and are by no means limited to the areas of application listed.

Complex oxides formed in binary systems such as Ln_2O_3: MeO_3 (Me–Mo, W) are of particular interest. This group of compounds has attracted considerable scientific interest following the discovery of the LAMOX family of compounds based on molybdate $La_2Mo_2O_9$, which exhibit outstanding oxygen conductivity values.[16–18] Further study of this family of compounds has enabled the creation of a variety of transport,[19,20] luminescent,[21–26] and photocatalytic[27] materials based on them.

[a] Y. V. Seredina, N. A. Khritokhin, N. O. Azarapin, P. O. Glukhova, N. A. Shelpakova, Y. G. Denisenko
School of Natural Sciences, University of Tyumen
Tyumen 625003, Russia
E-mail: yu.g.denisenko@gmail.com

[b] A. S. Oreshonkov
Laboratory of Molecular Spectroscopy, Kirensky Institute of Physics Federal Research Center KSC SB RAS, Krasnoyarsk 660036, Russia

[c] A. S. Oreshonkov
School of Engineering and Construction, Siberian Federal University, Krasnoyarsk 660041, Russia

[d] M. S. Molokeev
Laboratory of Crystal Physics, Kirensky Institute of Physics, Federal Research Center KSC SB RASK, Krasnoyarsk 660036, Russia

[e] M. S. Molokeev
Laboratory of Theory and Optimization of Chemical and Technological Processes, Tyumen State University, Tyumen 625003, Russia

[f] A. E. Sedykh, M. A. Zhernakov, K. Müller-Buschbaum, Y. G. Denisenko
Institute of Inorganic and Analytical Chemistry, Justus-Liebig-University Giessen, Giessen 35392, Germany

[g] A. S. Aleksandrovsky
Laboratory of Coherent Optics, Kirensky Institute of Physics Federal Research Center KSC SB RAS, Krasnoyarsk 660036, Russia

[h] A. S. Aleksandrovsky
Institute of Nanotechnology, Spectroscopy and Quantum Chemistry, Siberian Federal University, Krasnoyarsk 660041, Russia

[i] M. A. Zhernakov
A.M. Butlerov Chemistry Institute, Kazan Federal University, Kazan 420008, Russia

[j] K. Müller-Buschbaum
Center for Materials Research (LaMa), Justus-Liebig-University Giessen, Giessen 35392, Germany

[k] Y. G. Denisenko
Department of Construction Materials, Industrial University of Tyumen, Tyumen 625000, Russia

Supporting information for this article is available on the WWW under https://doi.org/10.1002/chem.202402084

Numerous publications are devoted to the study of structure and properties of phases in Eu_2O_3:MeO_3 (Me–Mo, W) systems. Namely, the formation processes, crystal structure, vibrational and luminescent properties of $Eu_2(MeO_4)_3$ (Me–Mo, W) compounds exhibiting a variety of structural features have been well and systematically studied.[28–36] In contrast, the compositions Eu_2MeO_6 and $Eu_2Me_2O_9$ are not thoroughly analyzed, since the main focus is on luminescent properties without a relation to structure-dependent parameters.[37,38]

Hence, this work is devoted to a systematic study of the thermodynamic and kinetic parameters of solid-phase reactions for the formation of the Eu_2MeO_6, $Eu_2Me_2O_9$ (Me–Mo, W) compounds. In addition, we present the study of their crystal and electronic structure, vibrational, optical, and luminescent properties. In the part of optical properties, we pay special attention to the investigation of the onset of fundamental absorption in the crystals under discussion. Recently it was shown that determination of a calculated optical band gap via the electronic band structure diagram could be a risky approach that leads to systematic errors. Moreover, it can result in the use of time- and hardware-consuming simulations.[39,40] For example, usage of hybrid functionals that may not be necessary to achieve good agreement with the experiment. Herein, we developed this approach with an application to the investigated materials and obtained conceptual agreement between *ab initio* simulated absorption spectra and experimental Kubelka-Munk functions. Moreover, we found that several improvements in *ab initio* simulation techniques may be useful to obtain quantitative agreement between *ab initio* simulated absorption spectra and experimental Kubelka-Munk functions.

Results and Discussion

Thermochemistry of Formation

The study of phase formation in binary oxide systems for the compositions $1Eu_2O_3$:$1MeO_3$ and $1Eu_2O_3$:$2MeO_3$ (Me–Mo, W) was carried out by Differential Thermal Analysis (DTA). In all cases, heat release corresponding to a one-stage interaction was recorded (Figure 1). The full DTA/TG curves for the heating and cooling processes are presented in Figure S1. According to X-ray phase analysis of the samples subjected to DTA, in the $1Eu_2O_3$:$1MeO_3$ (Me–Mo, W) and $1Eu_2O_3$:$2WO_3$ systems, such interaction results in the formation of single-phase samples Eu_2MeO_6 (Me–Mo, W) and $Eu_2W_2O_9$ (Figure S2 a,b,d). The chemical interactions between binary oxides are represented by the following Equations (1) and (2):

$$Eu_2O_3 + MeO_3 \rightarrow Eu_2MeO_6 \ (Me-Mo,\ W) \quad (1)$$

$$Eu_2O_3 + 2WO_3 \rightarrow Eu_2W_2O_9 \quad (2)$$

Interactions in the $1Eu_2O_3$:$2MoO_3$ system result in a three-phase sample consisting of $Eu_2(MoO_4)_3$, Eu_2MoO_6, and Eu_2O_3 (Figure S2 c), with the interaction being described by the Equation (3):

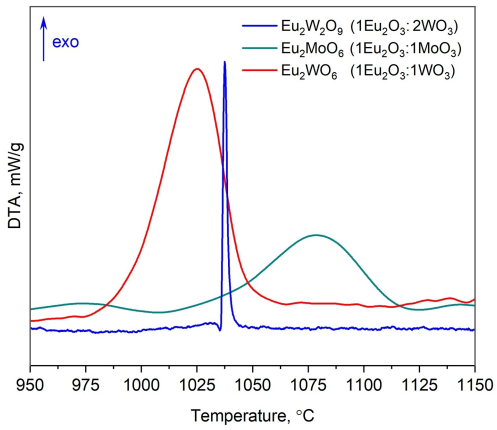

Figure 1. DTA curves of the interaction of simple oxides for the compositions $1Eu_2O_3$:$1MeO_3$ (Me–Mo, W) and $1Eu_2O_3$:$2WO_3$.

$$2Eu_2O_3 + 4MoO_3 \rightarrow Eu_2(MoO_4)_3 + Eu_2MoO_6 \quad (3)$$

It is reasonable to presume a two-stage mechanism of the process. However, according to DTA data, this is a single-stage process and is not the result of solid-phase decomposition. Long-term annealing (480 hours) of the $1Eu_2O_3$:$2MoO_3$ composition at temperatures of 500, 700, and 1000 °C did not result in a shift in the chemical equilibrium toward the formation of $Eu_2Mo_2O_9$, indicating the instability of this phase throughout the entire temperature range studied. We assume that the compound is unstable due to a strong stress in the crystal structure associated with the deformation of coordination polyhedra. It is logical to presume that an increase in the structure density during the transition from $Eu_2W_2O_9$ to $Eu_2Mo_2O_9$ leads to a greater distortion of the coordination polyhedra and stress in the structure, so the latter can no longer exist.

Table 1 presents the thermal, thermodynamic, and kinetic characteristics of the formation processes of the complex oxides. The dependences of the manifestation of heat release maxima on the heating rate are presented in Figure S3.

A distinctive feature of the studied systems is the formation of Eu_2MeO_6 compounds in a wide temperature range. By contrast, the formation of the $Eu_2W_2O_9$ compound occurs very rapidly in the range of only about 10 °C. This lability is not consistent with the high activation energy calculated from thermal analysis data obtained for different heating rates (Table 1). This may indicate that the formation of $Eu_2W_2O_9$ at these fairly high heating rates occurs through a more complex mechanism than Equation (2) suggests. Hence, we can propose a two-step process:

$$Eu_2O_3 + WO_3 \rightarrow Eu_2WO_6 \quad (4)$$

$$Eu_2WO_6 + WO_3 \rightarrow Eu_2W_2O_9 \quad (5)$$

However, at high heating rates, the separate consecutive formation of Eu_2WO_6 and $Eu_2W_2O_9$ does have little time to occur, and the overall unfavorable process (4-5) proceeds. From

Table 1. Temperature, thermodynamic and kinetic parameters of the formation of Eu_2MeO_6 (Me–Mo, W), and $Eu_2W_2O_9$ compounds.

Composition	Reaction	Temperature range of reaction, °C	ΔH, kJ/mol	Kinetic parameters		
				Kissinger equation		Ozawa-doyle equation
				E_A, kJ/mol	A	E_A, kJ/mol
$1Eu_2O_3$:$1MoO_3$	$Eu_2O_3 + MoO_3 \rightarrow Eu_2MoO_6$	1010–1125	−37	500	$4 \cdot 10^{16}$	456
$1Eu_2O_3$:$1WO_3$	$Eu_2O_3 + WO_3 \rightarrow Eu_2WO_6$	945–1065	−32	233	$3 \cdot 10^{6}$	245
$1Eu_2O_3$:$2WO_3$	$Eu_2O_3 + 2WO_3 \rightarrow Eu_2W_2O_9$	1035–1045	−24	6250	$6 \cdot 10^{247}$	5947

the thermal effects found (Table 1) it is apparent that the proposed step (5) is endothermic, 7 kJ/mol; thus, it is not only kinetically, but also energetically unfavorable. Then, the entropy of this stage is probably positive. We attribute it with a disorder associated with the conversion of symmetrical cubic fragments of [EuO_8] to less symmetrical two-capped [EuO_8] and three-capped [EuO_9] trigonal prisms. This phenomenon also corresponds to the transformation of the structure type from monoclinic base-centered to monoclinic primitive. Furthermore, this is supported by the fact that this unfavorable rearrangement of the coordination environment around europium is very diverse, and its activation entropy is very high, as evidenced by the high pre-exponential factor (Table 1).

Table 2. Main parameters of processing and refinement of the samples.

Compound	Eu_2MoO_6	Eu_2WO_6	$Eu_2W_2O_9$
Sp.Gr.	*C*2/*c*	*C*2/*c*	$P2_1/c$
a, Å	16.57463(12)	16.4536(3)	7.59554(6)
b, Å	11.22378(8)	11.22533(18)	9.73002(8)
c, Å	5.44560(4)	5.43273(9)	9.17275(7)
β, °	108.2478(4)	107.7034(7)	107.7640(3)
V, Å^3	962.009(12)	955.89(3)	645.601(9)
Z	8	8	4
2θ interval, °	7–140	7–140	7–140
R_{wp}, %	3.79	2.80	3.38
R_p, %	2.85	2.00	2.38
R_{exp}, %	2.32	1.47	1.54
χ^2	1.64	1.91	2.20
R_B, %	0.72	0.67	0.91

Crystal and Electronic Structure

High-resolution diffraction patterns are presented in Figure 2. All peaks of $Eu_2(Mo,W)O_6$ compounds were indexed by monoclinic cell (*C*2/*c*) with parameters close to Ln_2MoO_6[41] and all peaks of $Eu_2W_2O_9$ were indexed by monoclinic ($P2_1/c$) with parameters close to $Pr_2W_2O_9$.[42] Therefore, these structures were taken as starting models for Rietveld refinement, which was performed using TOPAS 4.2.[43] Sites of Ln ions were occupied by Eu ions. Refinements were stable and gave low R-factors (Table 2). Coordinates of atoms and main bond lengths are presented in Table S1 and Table S2, respectively.

The asymmetric part of the unit cells of $Eu_2(Mo,W)O_6$ contains two europium ions (Eu1, Eu2) in special sites (4e, local symmetry "2") and one Eu3 in a general site (4f), one molybdenum ion in general Wyckoff site and six O^{2-} ions in general sites. All Eu ions (Eu1, Eu2, Eu3) are coordinated by eight O^{2-} ions forming [EuO_8] cubes. The Mo ion is coordinated by five O^{2-} ions, forming a trigonal bipyramid (Figure 3a). The asymmetric part of the $Eu_2W_2O_9$ unit cell contains two europium ions, two tungsten ions, and nine O^{2-} ions, all in general sites. The Eu1 ion is coordinated by eight O^{2-} ions forming bicapped trigonal prism [EuO_8]. The Eu2 ion is coordinated nine-fold by a tricapped trigonal prism [EuO_9]. All tungsten ions are coordinated by six O^{2-} ions forming [WO_6] octahedra (Figure 3b).

Scanning electron microscopy (SEM) data indicates that polycrystalline samples of Eu_2MeO_6 (Me–Mo, W) compounds (Figure 4a, b) are predominantly formed by particles with a size of 0.5–1 μm, which are combined into agglomerates. The particles are predominantly faceted and exhibit a monoclinic

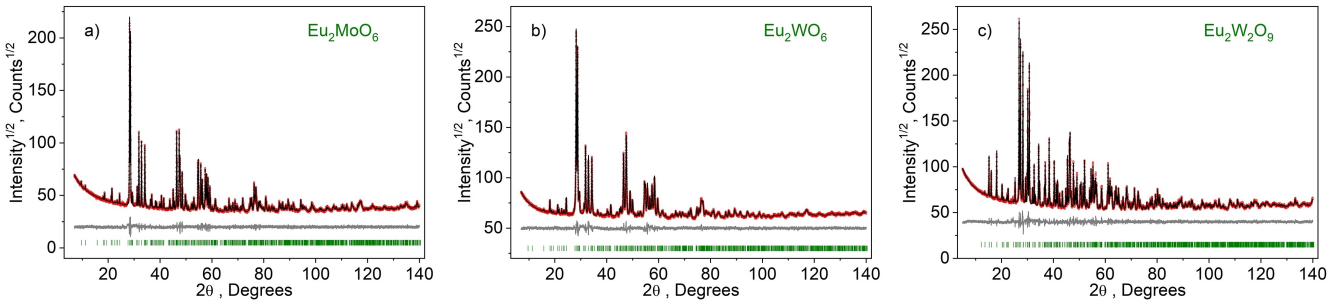

Figure 2. Difference Rietveld plot of Eu_2MoO_6 (a); Eu_2WO_6 (b); $Eu_2W_2O_9$ (c). (Red dots — experimental pattern Y_{obs}, black line — calculated pattern Y_{calc}, grey line — difference Y_{obs}-Y_{calc}, green bars — Bragg peaks).

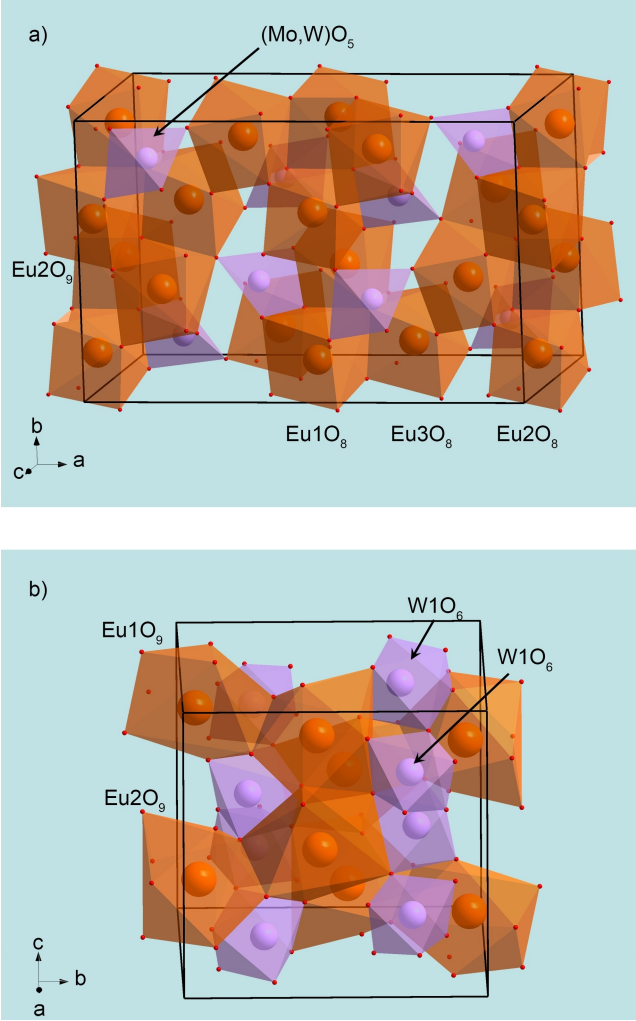

Figure 3. Crystal structures of $Eu_2(Me)O_6$ (Me–Mo, W) (a), $Eu_2W_2O_9$ (b).

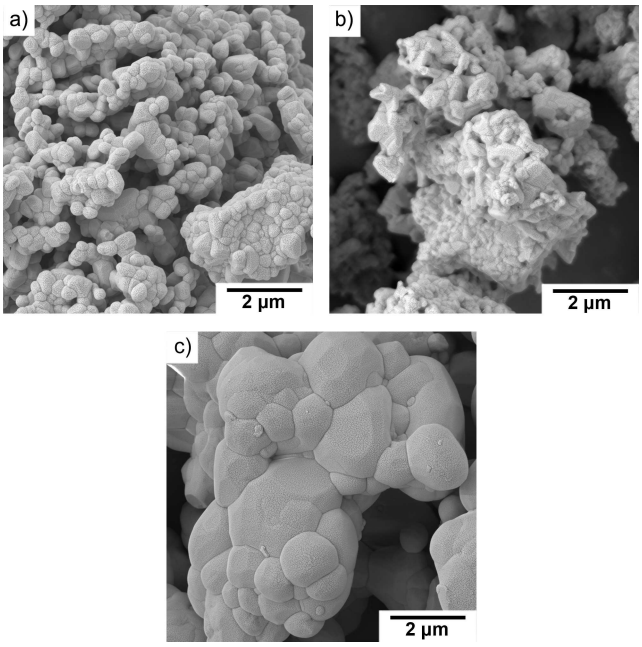

Figure 4. SEM images of Eu_2MoO_6 (a), Eu_2WO_6 (b), $Eu_2W_2O_9$ (c).

motif in their shape. A sample of the $Eu_2W_2O_9$ compound (Figure 4c) is formed by larger particles with sizes from 2 to 5 μm, in the structure of which a faceting and monoclinic motif can also be traced. Such a difference in particle size may be associated with a significant difference in the kinetic parameters of the formation processes, as well as with a difference in the diffusion mechanisms accompanying the interaction at the interface.

Figure 5 presents the Raman and infrared spectra of the investigated compounds, with vertical ticks denoting the calculated wavenumbers. Considering that Eu_2MoO_6 and Eu_2WO_6 are isostructural, similarities in their vibrational spectra are obvious. However, a transition metal is surrounded by five oxygen ions (forming a trigonal bipyramid) in Eu_2MeO_6, whereas in $Eu_2W_2O_9$ it is surrounded by six oxygen ions (forming an octahedron), the spectra of these compounds differ significantly. The high-wavenumber (between 800 and 900 cm^{-1}) high-intensity lines in the Raman spectra of Eu_2MeO_6 are associated with Me–O symmetric stretching (Figure 6a). The region of 670–770 cm^{-1} is associated with antisymmetric stretching in trigonal bipyramids (Figure 6b). A similar high-wavenumber range in the infrared spectra corresponds to the same types of vibrations, but these vibrations are antisymmetric relative to the lattice. In other words, while part of the polyhedra undergoes compression, then the another part undergoes expansion. The strong high-intensity band at

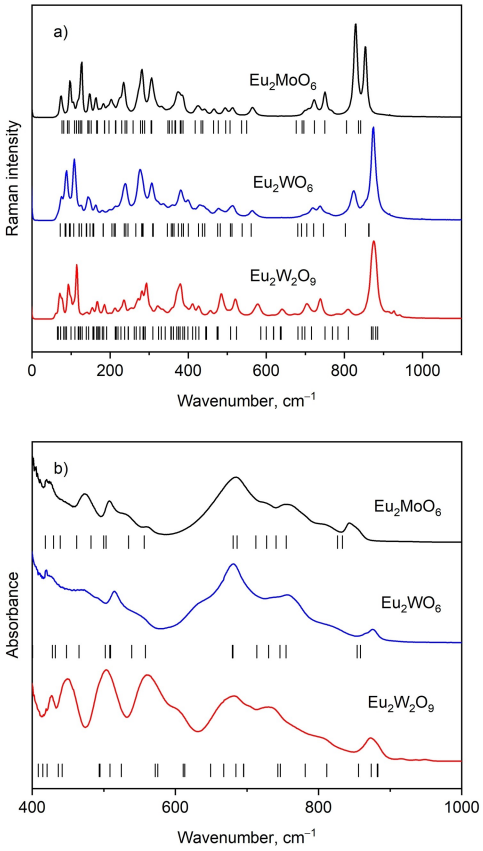

Figure 5. Raman (a) and infrared (b) spectra of Eu_2MoO_6, Eu_2WO_6 and $Eu_2W_2O_9$. The wavenumber positions of vibrational modes are shown by black bars.

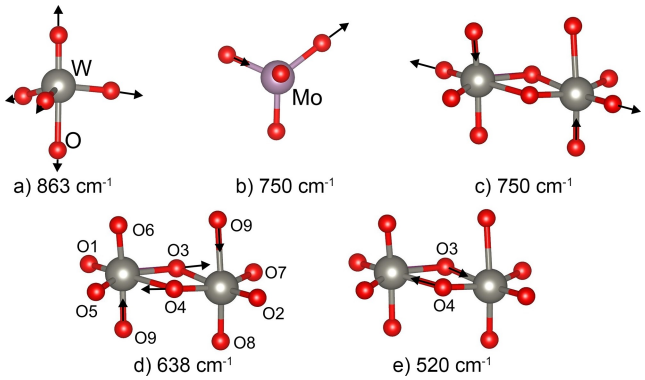

Figure 6. Geometric representation of vibrations discussed in the text for Eu_2WO_6 (a), Eu_2MoO_6 (b) and $Eu_2W_2O_9$ (c–e).

876 cm^{-1} in the Raman spectra of $Eu_2W_2O_9$ is associated with W–O stretching in [WO_6] octahedral. In particular, Figure 6c shows an example of antisymmetric W–O stretching. This example specifically demonstrates how these vibrations proceed, considering that the [WO_6] units are interconnected with each other. The presence of such structural features results in the appearance of characteristic bands, for example at 641 cm^{-1}, as presented in Figure 6d.

The intricate geometry of the polyhedra, coupled with their interconnection, presents challenges in graphical interpretation.

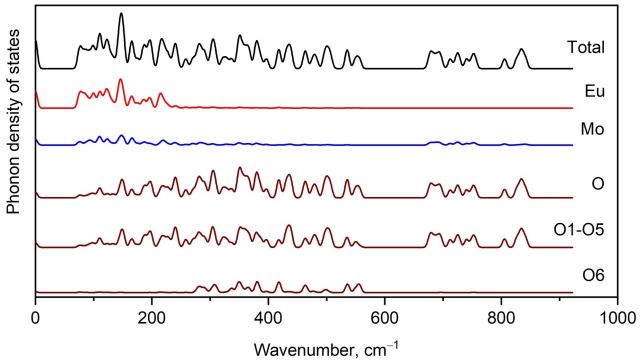

Figure 7. Total and partial phonon density of states in Eu_2MoO_6.

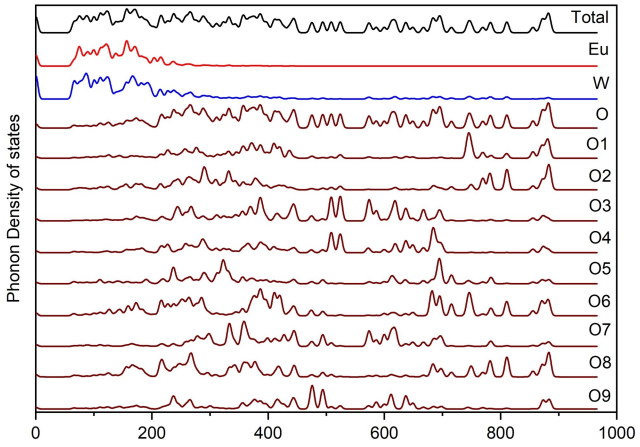

Figure 8. Total and partial phonon density of states of $Eu_2W_2O_9$.

One approach to addressing this is to utilize the phonon density of states. Figure 7 represents that only oxygen ions located in the [MoO_5] polyhedra of Eu_2MoO_6 vibrate in the region of 670–840 cm^{-1}. The region between 270 and 570 cm^{-1} in Figure 7 is also characterized by displacements of O6, which indicates vibrations of oxygen in the [EuO_9] polyhedra. Figure 7 clearly shows that peaks lower 100 cm^{-1} in Raman spectra (Figure 5a) of Eu_2MoO_6 are translations of the heaviest ions (Eu). Phonon density of states for Eu_2WO_6 is shown in Figure S4.

The unit cell of $Eu_2W_2O_9$ contains nine independent oxygen ions, and the phonon density of states for each of them is presented in Figure 8. Here, the O atoms are labeled in accordance with Table 2, with the same notation being used in Figure 6d. Thus, it is evident from Figure 8 that the geometry of vibration shown in Figure 6d corresponds to peaks for the O9, O4, and O3 ions. As an example, we show which ions contribute to the formation of the peak at 520 cm^{-1} in the Raman spectrum of $Eu_2W_2O_9$. Two bands for O3 and O4 ions can be observed in Figure 8; thus, the corresponding spectral line is associated with the movements of ions belonging to two [WO_9] octahedra. In particular, Figure 6e demonstrates the corresponding geometric representation.

Figure 9 shows the electronic structure. The path along high-symmetry points of the Brillouin zone should be chosen as follows: Γ–C | C_2–Y_2–Γ–M_2–D | D_2–A–Γ | L_2–Γ–V_2 which is shown in Figure S5. Based on the results of the meta-GGA method, the minimum value of electronic transitions is calculated to be 1.7 eV. However, this value underestimates the experimentally observed band gap. To address this discrepancy, the 'scissors' operator with a value of 1.3 eV was employed, and the resulting band structure is depicted in Figure 9. As europium is a lanthanide element, the spin up and spin down states are represented by different colors. According to Figure 9, we can consider Eu_2MoO_6 as an indirect band gap semiconductor. It should be noted that the magnitude of indirect and direct transitions is very close; however, the value of the direct optical transition (Γ–Γ) differs slightly in magnitude from the indirect one.

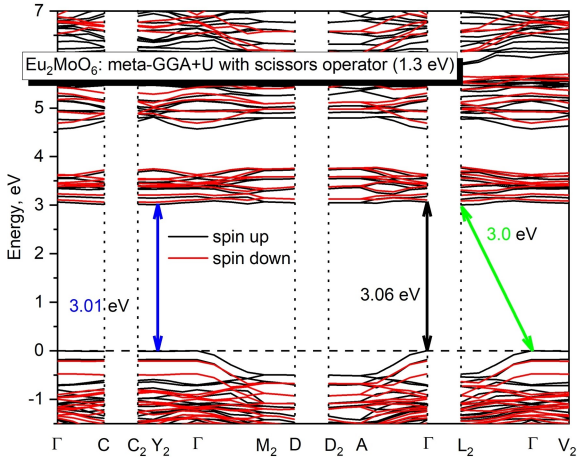

Figure 9. Electronic structure of Eu_2MoO_6.

The total electronic density of states (DOS) and the partial DOS are presented in Figure 10. Figure 10 shows that the top of the valence band of Eu_2MoO_6 is formed by the *p*-electrons of oxygen. The group of electronic branches between 3 and 4 eV is formed by the *d*-electrons of molybdenum. The subsequent group of bands in Figure 9 represents hybridized *d*–Mo and *p*–O electrons, as well as contributions from the *d*-electrons of europium, which can be found in this region. Based on the calculated band structure, the spectral dependencies of the absorption coefficients were determined and compared with experimental Kubelka-Munk functions. Figure 11 presents Kubelka-Munk functions (KMF) modified for direct and indirect band gaps. In particular, the experimental band gap values are $E_g^d = 3.37$ eV and $E_g^i = 3.13$ eV. Comparison of the experimental KMFs with calculated absorption spectra transformed by the Tauc procedure and with DOS (see Figure 10) shows that the experimental fundamental absorption band contains contributions which can be easily assigned to transitions to Mo *4d* states (in the range of 3–4.5 eV) and to Eu *5d* states (in the range above 4.5 eV).

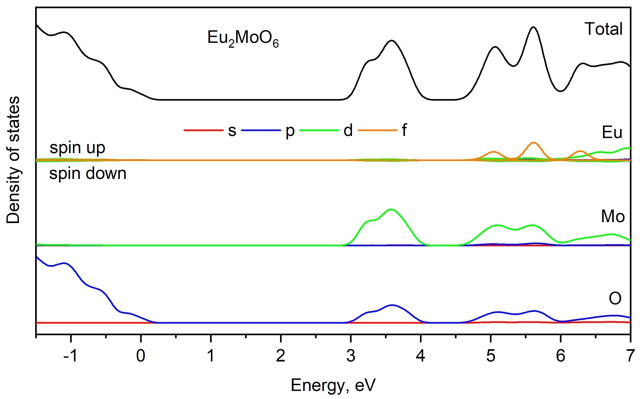

Figure 10. Total and partial density of electronic states for Eu_2MoO_6.

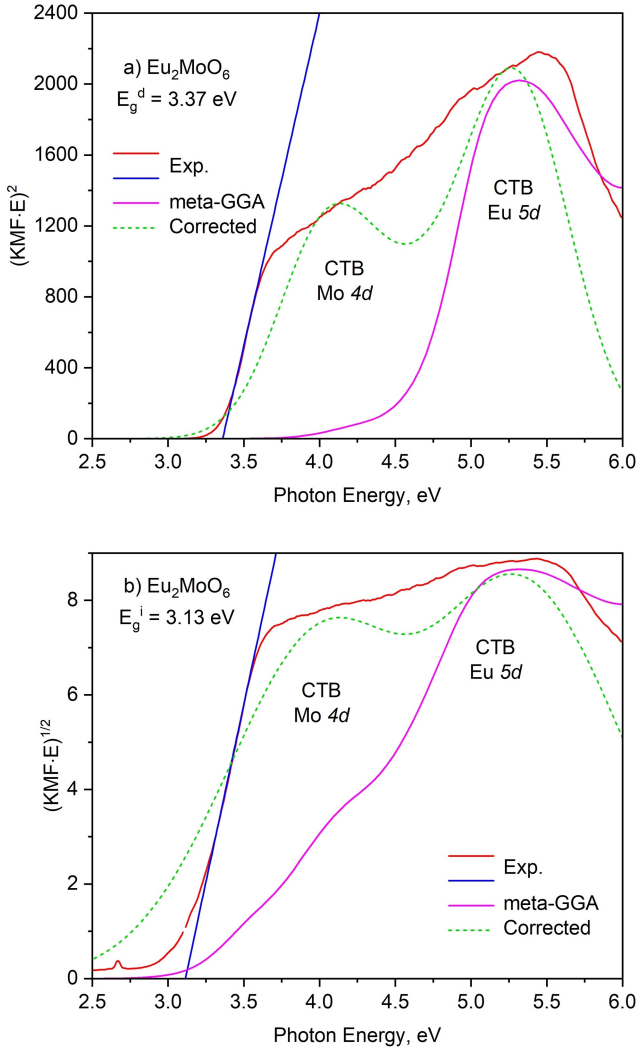

Figure 11. Kubelka-Munk function of Eu_2MoO_6 modified for direct band gap (a) and for indirect band gap (b) in comparison with meta-GGA calculations and with those corrected in part of Mo CTB probability.

However, the transition probabilities implemented in the DFT code used do not allow choosing such a scaling coefficient between the calculated absorption and experimental KMF that would equally satisfy the Mo and Eu charge transfer bands. The green lines in Figure 11 show the result of the above mentioned probability correction. In particular, a pair of Gaussians simulates CTB contours, with the probability of transitions to Mo *4d* states being provisionally multiplied by 10. This procedure does not claim to achieve an agreement between experiment and calculations, but rather demonstrates the potential possibility to obtain such agreement when more advanced simulation packages (if such exist) are used.

Figure 12 presents the calculated electronic band structure for Eu_2WO_6. Since Eu_2WO_6 is isostructural to Eu_2MoO_6, the path through the high-symmetry Brillouin zones is chosen in a similar manner to the molybdate discussed previously. From Figure 12, it can be derived that this tungstate is a wide-band gap indirect semiconductor, with a small difference between the indirect and direct transitions. The difference between the direct transition at the Y_2 point and the optical transition is only apparent in the second decimal place. To achieve the best agreement with the experimental data, a scissors operator of 0.6 eV was applied.

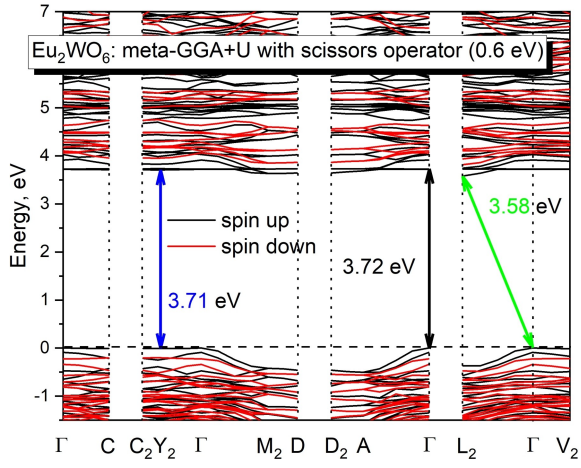

Figure 12. Calculated electronic band structure of Eu_2WO_6.

The total and partial DOS of Eu_2WO_6 are shown in Figure 13. It is evident from the figure that the contribution of O–*p* electrons is dominant in the valence region below the Fermi level. Meanwhile, *d*-electrons of tungsten mainly contribute the bottom of the conduction band. Additionally, we can note that hybridization of electronic states between W and O takes place, which is associated with the presence of tungsten-oxygen structural units.

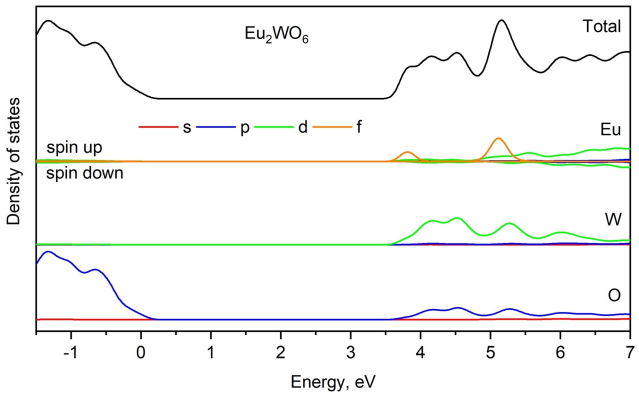

Figure 13. Total and partial density of electronic states for Eu_2WO_6.

The calculated Eu_2WO_6 band structure was used to compute the spectral dependence of the absorption coefficient, which was then compared to the experimental Kubelka-Munk functions. Figure 14 presents the Kubelka-Munk functions (KMF) of Eu_2WO_6 modified for direct and indirect band gaps. Experimental band gap values are $E_g^d = 3.59$ eV and $E_g^i = 3.85$ eV which are in a fair agreement with the data in Figure 12. Comparison of the experimental KMFs with the calculated absorption spectra transformed using the Tauc procedure and with the DOS (see Figure 13) shows that the experimental fundamental absorption band contains contributions that can be attributed to transitions to W *5d* states (in the range of 4–5 eV) and to Eu *5d* states (in the ranges near 4 eV and above 5 eV). As previously stated, the transition probabilities implemented in the DFT code used do not allow us to select a scaling coefficient between calculated absorption and experimental KMF. Thus, green lines in Figure 14 show the result of the correction of probabilities mentioned above. In particular, a pair of Gaussians simulates CTB contours, with the probability of transitions to W *5d* states being provisionally multiplied by 8.33. This procedure, as in the case of Eu_2MoO_6, does not purport to obtain an agreement between experiment and calculations but merely illustrates the potential possibility to obtain such agreement in case of using more advanced (if such exist) simulation packages. The 'scissors' operator was not used in the case of Eu_2WO_6, though the simultaneous use of scissors operator and probability correction would probably further improve the consistency between the experimental KMF and the calculations.

Figure 15 represents the calculated electronic structure for $Eu_2W_2O_9$. The path along the high symmetry points of the Brillouin zone was chosen as follows: G–Z–D–B–G–A–E–Z–C_2–Y_2–G, which is illustrated in Figure S6. In this case, the meta-GGA + U model was used and no scissors operator was applied. According to Figure 15, the following electronic transitions can be listed: a direct G–G transition to a highly dispersive branch

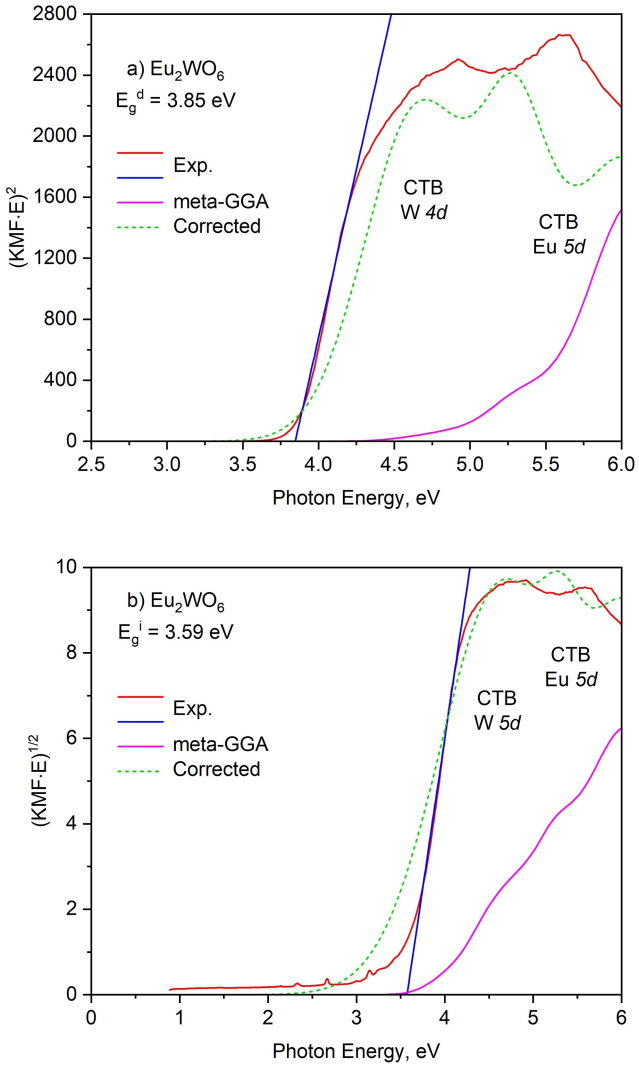

Figure 14. Kubelka-Munk Function of Eu_2WO_6 modified for direct band gap (a) and for indirect band gap (b) in comparison with meta-GGA calculations and with those corrected in part of W CTB probability.

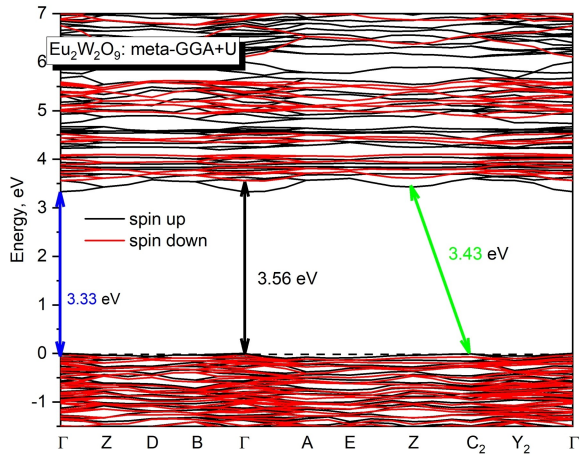

Figure 15. Electronic structure of $Eu_2W_2O_9$.

in the bottom of the valence band (3.33 eV), an indirect C_2-Z transition (3.43 eV), and a direct G–G transition equal to 3.56 eV.

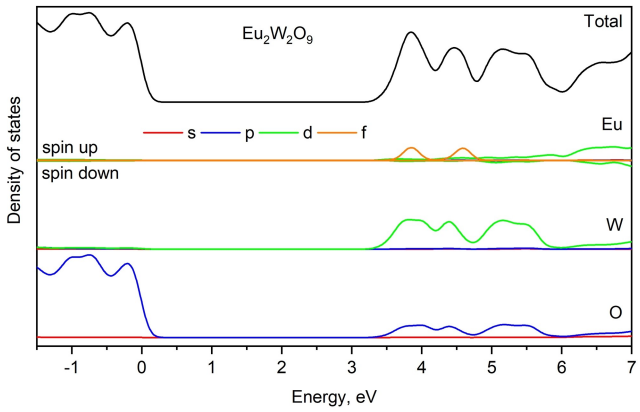

Figure 16. Total and partial density of electronic states for $Eu_2W_2O_9$.

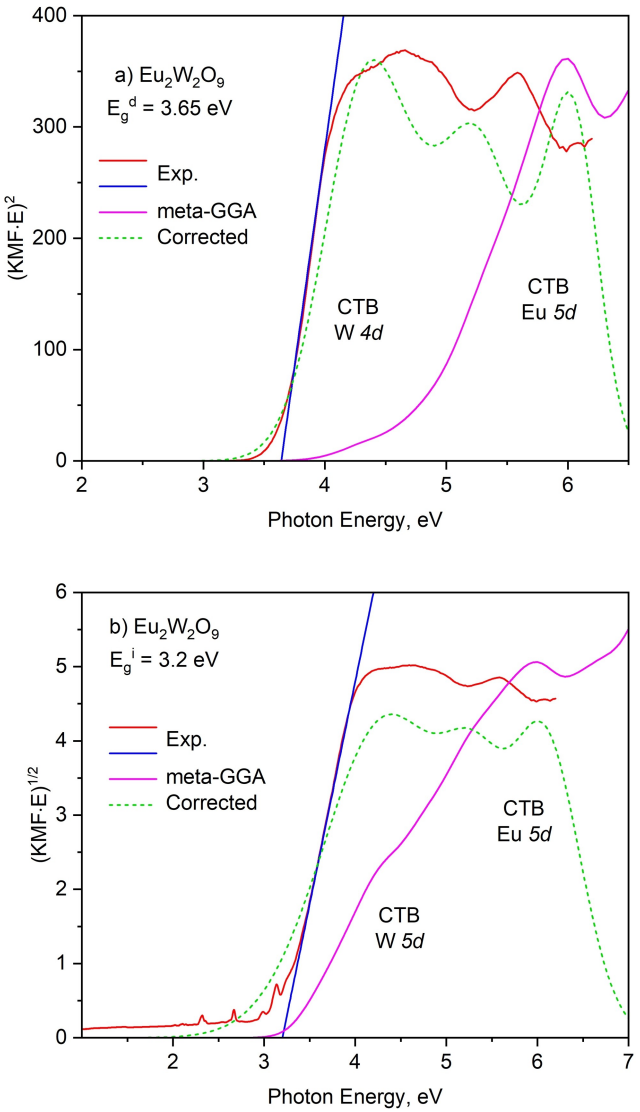

Figure 17. Kubelka-Munk function of $Eu_2W_2O_9$ modified for direct band gap (a) and for indirect band gap (b) in comparison with meta-GGA calculations and with those corrected in part of W CTB probability.

The total and partial density of states (DOS) calculated for $Eu_2W_2O_9$ can be seen in Figure 16. An analysis of Figure 16 revealed that below the Fermi level O–*p* electrons predominantly influence the valence region. Likewise in Eu_2WO_6, the lower part of the conduction band is primarily affected by *d*-electrons of W. Furthermore, we want to emphasize that the density of electronic states below the Fermi level differs between $Eu_2W_2O_9$ and Eu_2WO_6, indicating variations in the configuration of the $WO_{5\text{-}6}$ structural units and contributing to a decreased band gap value in the case of $Eu_2W_2O_9$.

The band gap values for $Eu_2W_2O_9$ that can be extracted from Figure 15 are quite close to the experimental values of the direct band gap $E_g^d = 3.65$ eV and the indirect band gap $E_g^i = 3.2$ eV, which are presented in Figure 17 together with meta-GGA calculations of the absorption spectrum. In the case of $Eu_2W_2O_9$, we applied the correction, which required a multiplication of the probability of the transitions to the lowest W *5d* states by a factor of 4.8. In addition, several minor corrections were applied to the upper subbands to obtain the corrected curve in Figure 17.

Luminescent Properties

The luminescent properties of Eu^{3+} ions doped in different molybdate and tungstate hosts and the possibility of controlling the excitation spectra in order to adjust them to the range of efficient generation of GaInN LEDs were studied before.[44] The excitation spectra of the host studied in that paper contained charge transfer bands of [MoO_x] and [WO_x] groups suitable for pumping by LEDs, which loosens the LED wavelength stability requirements arising in the case of pumping via narrow *f-f* lines of Eu^{3+} ion. It was established that the charge transfer band (CTB) edge can be tuned between 300 and 480 nm using lattice engineering. In particular, it was found that the phosphors $Me1Me2O_4$:Eu^{3+} (Me1 – Ca, Sr, Ba; Me2 – Mo, W) with the absorbing group [$M2O_4$] are characterized by CTB below 330 nm while Ln_6MoO_{12}: Eu^{3+} (Ln – Y, Gd) with the absorbing group [MoO_6] have CTB edge at 480 nm.[44]

In the present study, Eu_2MeO_6 crystals were investigated that are the limiting case of Ln_2MoO_6:Eu^{3+} (Ln—Y, Gd) for Eu content approaching 100%; both of them contain [MoO_5] absorbing groups which are characterized by 400 nm CTB edge in the case of Ln_2MoO_6:Eu^{3+}. Excitation spectra for emission wavelengths at $^5D_0 \rightarrow {}^7F_2$ transition are presented in Figure 18.

The CTB in Eu_2MoO_6 is similar to that observed in Ln_2MoO_6:Eu^{3+}. The specific feature of Eu_2MoO_6 is the presence of additional CTB belonging to O^{2-} – Eu^{3+}, which should not be observed in Ln_2MoO_6:Eu^{3+} due to the low Eu^{3+} content. The CTB in Eu_2WO_6 is of lower amplitude than for Eu_2MoO_6 and is shifted to the shorter wavelengths, with a maximum at 310 nm. The CTB in $Eu_2W_2O_9$ is even weaker than in Eu_2WO_6 and exhibits two maxima, despite two inequivalent positions of W in the crystal structure of $Eu_2W_2O_9$ are of similar geometry being coordinated by 8 oxygen atoms. Therefore, we can assign the longer-wavelength CTB in $Eu_2W_2O_9$ to the [WO_6] group and the shorter-wavelength band to Eu^{3+} – O^{2-} CTB.

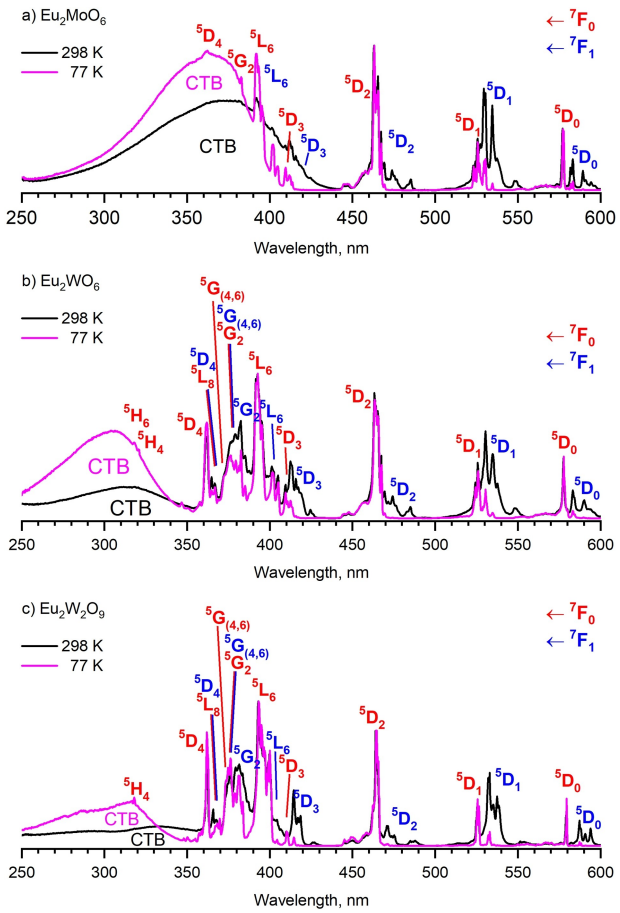

Figure 18. Excitation spectra for emission wavelengths at $^5D_0 \rightarrow {}^7F_2$ transition at room temperature.

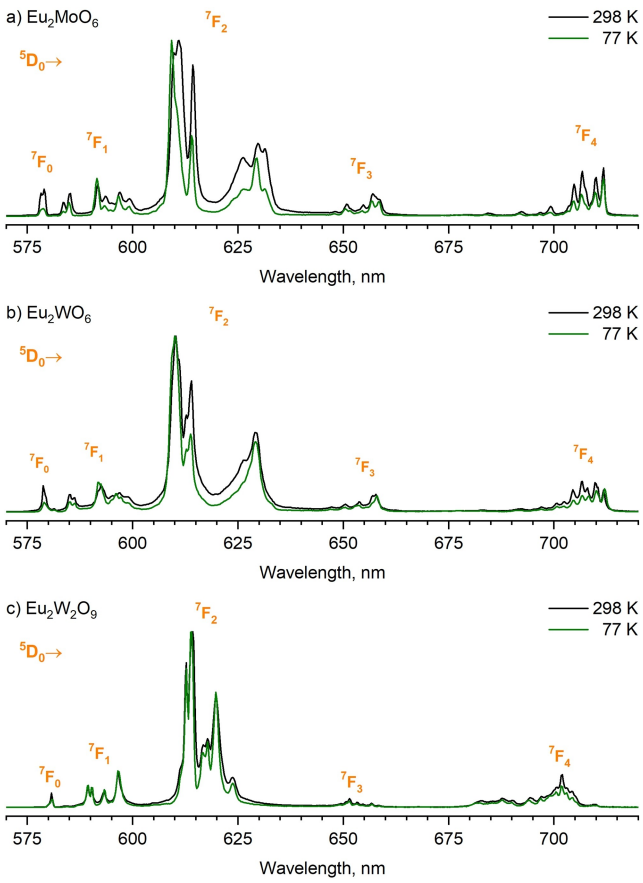

Figure 19. Luminescence spectra due to emission from $^5D_0$ state of Europium ion at room temperature.

The excitation spectra of three investigated crystals undergo different modification upon cooling to 77 K. The example of such modification for Eu_2MoO_6 is presented in Figure 18a. Upon cooling, the bands corresponding to the *f-f* transitions of the Eu^{3+} ion undergo a reduction of longer-wavelength components, which can be explained by the devastation of thermally populated upper energy levels of the spin-orbit-split ground state that noticeably contribute to the excitation spectrum only at room temperature. Additionally, CTB experiences similar reduction of the longer wavelength component; the mirror counterpart of this phenomenon is well-investigated for the case of heating the crystals containing the absorbing group VO_4^{3+}.[45] This type of CTB was employed for thermometry[46] with the sensitivity of $3313/T^2$, which is greater than a lot of thermometers based on paired emissions of down-converting rare earth ions. For Eu_2MoO_6, the CTB to a discrete *f-f* line ratio can be used for thermometry, too. The most temperature-dependent part of the CTB in Eu_2MoO_6 lies in the wavelength range of 420–440 nm.

Emission spectra of Eu_2MoO_6, Eu_2WO_6 and $Eu_2W_2O_9$ at room temperature and 77 K are presented in Figure 19. The spectra are practically independent of the excitation wavelength and show negligible variations at excitation wavelengths of 333, 393 and 464 nm.

In particular, this means that excitation through CTB eventually leads to the energy transfer terminating at the $^5D_0$ state of the Eu^{3+} ion, which is the starting level for the spectra.

The Eu^{3+} ions occupy three inequivalent sites in the *C*2/*c* group, the local symmetry being C_2 for two of them and C_1 for the third one, and two inequivalent sites in the $P2_1/c$ group, the local symmetry for both being as low as C_1. These local symmetries imply both the observability of the ultranarrow $^5D_0 \rightarrow {}^7F_0$ line (579.5 ± 1.5 nm) and the absence of the inversion symmetry that induces the electric dipole moment at the hypersensitive $^5D_0 \rightarrow {}^7F_2$ transition (605–635 nm). The spectra presented in Figure 19 are consistent with these predictions. However, only two of three possible ultranarrow lines can be detected for both crystals belonging to *C*2/*c* group (e.g., at 578.1 and 578.8 nm for Eu_2MoO_6) and only one ultranarrow line for $Eu_2W_2O_9$ at 580.75 nm. The undetected ultranarrow lines probably coincide with the detected ones within the spectral resolution used.

Experimental Section

Synthesis

The synthesis was carried out using solid-state reactions:

$$Eu_2O_3 + MeO_3 \rightarrow Eu_2MeO_6 \quad (6)$$

$$Eu_2O_3 + 2MeO_3 \rightarrow Eu_2Me_2O_9 \quad (7)$$

For the synthesis, high-purity starting reagents Eu_2O_3 (99.999%, RedkiyMetallRF ltd., Ekaterinburg, Russia), MoO_3 (99.9%, Vekton ltd., St. Petersburg, Russia) and WO_3 (99.9%, Vekton ltd., St. Petersburg, Russia) were used. Prior to synthesis, the oxides were annealed to remove moisture and carbon dioxide for 12 hours. Eu_2O_3 and WO_3 were annealed at a temperature of 1000 °C, while MoO_3 was annealed at 600 °C. The oxides were weighed on an analytical balance with an accuracy of 0.1 mg. The stoichiometric oxide mixture was thoroughly ground in an agate mortar for 20 minutes, and then transferred to a corundum crucible. The crucible was placed in a muffle furnace at 900 °C and kept for 12 hours. The heat-treated sample was thoroughly ground in an agate mortar and subjected to a repeated heating process for 12 hours. The degree of conversion and phase composition of the samples were controlled by X-ray phase analysis.

Physical and Physico-Chemical Methods

The X-ray diffraction (XRD) for phase analysis was performed on a BRUKER D2 PHASER diffractometer with a linear detector LYNXEYE (CuK_α radiation, Ni filter). The Rietveld refinements of the selected samples were performed using TOPAS 4.2 software package.[43] The powder diffraction data for Rietveld structural analysis collected at room temperature with a Bruker D8 ADVANCE powder diffractometer (CuK_α radiation) and linear VANTEC detector. The step size of 2θ was 0.016° and the counting time was 5 s per step.

The crystallographic data are deposited in Cambridge Crystallographic Data Centre (CSD # 2358351–2358353). The data can be downloaded from the site (www.ccdc.cam.ac.uk/data_request/cif).

The electron microscopy analysis was carried out on an electron microscope JEOL JSM-6510LV.

Thermal analysis was carried out in an argon flow using the Differential Thermal Analysis (DTA/TG) equipment 499 F5 Jupiter NETZSCH (Netzsch, GmbH & Co. KG, Hamburg, Germany). The powder samples were inserted into alumina crucibles. The heating rate was 3 °C/min. For enthalpy determination, the equipment was calibrated with the use of standard substances, such as In, Sn, Bi, Zn, Al, Ag, Au, and Ni. The heat effect peaks were determined using the Proteus 6 2012 software. The peak temperatures and areas in the parallel experiments were reproduced with an inaccuracy of less than 3%. The determination of the kinetic parameters was based on the Kissinger Equation (8)[47,48] in linearized form and on the Ozawa – Doyle Equation (9):[49,50]

$$-\frac{1}{T} = \frac{1}{E} R \ln \frac{b}{T^2} - \frac{R}{E} \ln \frac{AR}{E} \quad (8)$$

$$\lg\beta + \frac{0.4567E}{RT} = C \quad (9)$$

where T is the temperature at the maximum reaction rate, b is the heating rate, E is the activation energy, A is the pre-exponential factor, R is the gas constant, and C is the constant.

The Fourier-transform infrared spectroscopy (FTIR) analysis was carried out on a Fourier Transform Infrared Spectrometer FSM 1201. The sample for the investigation was prepared in a tablet shape with the addition of annealed KBr. Raman spectra were recorded using an i-Raman Plus spectrometer at a laser excitation wavelength of 785 nm.

For the photoluminescence investigations, the sample was mortared, filled into a quartz glass cuvette, and examined at room temperature and at 77 K (using a special liquid nitrogen-filled Dewar assembly). The spectra were recorded on a Horiba Jobin Yvon Spex Fluorolog 3 spectrophotometer equipped with a 450 W Xe short-arc lamp (USHIO), double-grated excitation and emission monochromators, a photomultiplier tube (R928P), and a TCSPC upgrade using the FluoroEssence software. Both the excitation and emission spectra were corrected for the spectral response of the monochromators and detector using spectral corrections provided by the manufacturers. The excitation spectra were additionally corrected for the spectral distribution of the lamp intensity by use of a photodiode reference detector.

All density functional theory (DFT) calculations were carried out using the Cambridge Serial Total Energy Package (CASTEP code).[51] The meta-generalized gradient approximation including the on-site orbital dependent Hubbard U energy term[52] and the RSCAN[53] functional (an improved version of the SCAN[54]) were selected. The values of U for lanthanides and Mo were taken as $U(f) = 7$ eV and $U(d) = 3.5$ eV, respectively.[55] Norm-conserving pseudopotentials were generated on-the-fly in CASTEP, with a cutoff energy set to 816.3 eV. The Brillouin zone (BZ) was sampled by the 2×2×4 and 3×2×2 Monkhorst-Pack k-meshes for $Eu_2(Mo,W)O_6$ and $Eu_2W_2O_9$, respectively. The convergence criterion for minimization of total energy was set to be 1×10^{-8} eV.[56]

Conclusions

Studying the formation mechanisms and structures of compounds is an important task in modern solid state chemistry, as it allows us to better understand the patterns associated with the targeted production of materials with specific properties. In this study, we accumulate and discuss extensive theoretical and experimental investigations on the compounds Eu_2MoO_6, Eu_2WO_6, and $Eu_2W_2O_9$. The presented complex compounds were obtained from solid-phase reactions between simple oxides. Thermodynamic and kinetic characteristics were established for all reactions, and a mechanism was proposed to explain their significant differences. The simplicity of the synthesis method ensures its high reproducibility and selectivity. The compounds were characterized by X-ray diffraction analysis, vibrational, ultraviolet and luminescent spectroscopy. The absence of contradictions in the results obtained using research methods based on various physical principles determines the reliability of this study. The study has revealed that the electronic structure of the compounds Eu_2WO_6 and $Eu_2W_2O_9$ is characterized by a significant contribution of electrons from different elements, predominantly O–*p* and W–*d*, to the valence and conduction bands, respectively. The hybridization of electronic states between W and O indicates the presence of tungsten-oxygen structural units in these compounds. A comparison between experimental data and calculated absorption values emphasized the need for transition probability corrections to achieve the agreement between them. The DFT calculations demonstrated the significant influence of $[WO_5]$ and $[WO_6]$ geometry on the band gap width and electronic

density of states in Eu_2WO_6 and $Eu_2W_2O_9$ compounds, respectively. Analysis of the luminescent properties suggests the potential use of the Eu_2MeO_6 and $Eu_2W_2O_9$ compounds as thermometers in optical thermal sensing. The dependence of the luminescence spectra on the excitation wavelength opens up possibilities for controlling and tuning the spectra in various technological applications. Overall, results of this research provide a better understanding and utilization of the electronic and optical properties of Eu_2MeO_6 and $Eu_2W_2O_9$ compounds in various scientific and technological fields. Further research and development may lead to new innovative applications of these compounds as optical, catalytic, and solid oxide fuel cell materials.

Supporting Information Summary

The supporting information contains sample diffraction patterns, dependences of heat release maxima on the heating rate, tables with factional atomic coordinates, and main bond lengths, Brillouin zones, and total and partial phonon density of states for Eu_2WO_6.

Acknowledgements

This work was partially performed using resources of the Research Resource Center "Natural Resource Management and Physico-Chemical Research" (University of Tyumen) and Krasnoyarsk Regional Center of Research Equipment of Federal Research Center "Krasnoyarsk Science Center SB RAS". We acknowledge Lisa-Marie Wagner (JLU Giessen) for help with X-ray powder diffraction, and Svetlana Volkova and Irina Palamarchuk (University of Tyumen) for help with IR and UV spectrometry. The work was partly carried out within the framework of the Strategic Academic Leadership Program "Priority-2030" for the Tyumen State University, Kazan Federal University, and Siberian Federal University and the state assignment of the Kirensky Institute of Physics.

Conflict of Interests

The authors declare no conflict of interest.

Data Availability Statement

Deposition Number(s) 2358351-2358353 contain(s) the supplementary crystallographic data for this paper. These data are provided free of charge by the joint Cambridge Crystallographic Data Centre and Fachinformationszentrum Karlsruhe Access Structures service.

Keywords: DFT · Europium · Molybdenum · Oxides · Tungsten

[1] J. E. Garcia, F. Rubio-Marcos, *Appl. Phys.* **2020**, *127*, 131102.
[2] A. Soukiassian, W. Tian, D. A. Tenne, X. X. Xi, D. G. Schlom, N. D. Lanzillotti-Kimura, A. Bruchhausen, A. Fainstein, H. P. Sun, X. Q. Pan, A. Cros, A. Cantarero, *Appl. Phys. Lett.* **2007**, *90*, 042909.
[3] H. Xiao, W. Dong, Y. Guo, Y. Wang, H. Zhong, Q. Li, M.-M. Yang, *Adv. Mater.* **2018**, *31*(4), 1805802.
[4] S. Walia, S. Balendhran, H. Nili, S. Zhuiykov, G. Rosengarten, Q. Wang, M. Bhaskaran, S. Sriram, M. Strano, K. Kalantar-zadeh, *Prog. Mater.* **2013**, *58*(8), 1443–1489.
[5] Y. Yin, B. Tudu, A. Tiwari, *Vacuum* **2017**, *146*, 356–374.
[6] N. Abanti, V. Shubha, *J. Electron. Mater.* **2014**, *43*, 962–977.
[7] G.-K. Ren, J. Lan, C. Zeng, Y. Liu, *Jom.* **2015**, *67*, 211–221.
[8] Y. Yu, L. Ma, P. Cai, R. Zhong, C. Ye, J. Shen, G. D. Gu, H. C. Xian, Y. Zhang, *Nature.* **2019**, *575*(7781), 156–163.
[9] Y. Zhang, X. Xu, *Comput. Mater. Sci.* **2020**, *179*, 109583.
[10] X. J. Chen, *MRE.* **2020**, *5*(6), 068102.
[11] R. Witte, S. Abhishek, R. Kruk, B. Eggert, R. Brand, H. Wende, H. Hahn, *Phys. Rev. Materials.* **2019**, *3*, 034406.
[12] M. Jeon, M. V. Halbert, Z. R. Stephen, M. Zhang, *Adv. Mater.* **2021**, *33*(23), 1906539.
[13] W. Fu, J. Yi, M. Cheng, Y. Liu, *J. Hazard. Mater.* **2022**, *424*, 127419.
[14] J. C. Vedrine, *Chin. J. Catal.* **2019**, *40*(11), 1627–1636.
[15] J. Amsler, B. B. Sarma, G. Agostini, G. Prieto, P. N. Plessow, F. Studt, *JACS.* **2020**, *142*(11), 5087–5096.
[16] N. Mhadhbi, W. Jabeur, A. Guesmi, A. Houas, B. N. Hamadi, H. Naïli, *RSC Adv.* **2023**, *13*, 30168–30175.
[17] E. I. Orlova, T. A. Sorokin, A. Antipin, E. P. Kharitonova, N. V. Lyskov, N. I. Sorokina, V. I. Voronkova, *Cryst. Growth Des.* **2022**, *23*(1), 473–479.
[18] E. I. Orlova, E. P. Kharitonova, N. I. Sorokina, T. A. Sorokin, A. M. Antipin, V. I. Voronkova, *Crystallogr. Rep.* **2020**, *65*, 697–703.
[19] R. Haugsrud, *Solid State Ionics.* **2007**, *178*(7–10), 555–560.
[20] N. Pestereva, A. Guseva, I. Vyatkin, D. Lopatin, *Solid State Ion.* **2017**, *301*, 72–77.
[21] C. A. Kodaira, H. F. Brito, M. C. F. C. Felinto, *J. Solid State Chem.* **2003**, *171*(1–2), 401–407.
[22] M. Fangui, X. Zhang, H. LI, J. S. Hyo, *J. Rare Earth.* **2012**, *30*(9), 866–870.
[23] M. Colmont, P. Boutinaud, C. Latouche, F. Massuyeau, M. Huvé, A. Zadoya, S. Jobic, *Inorg. Chem.* **2020**, *59*(5), 3215–3220.
[24] H. Gong, S. Shi, J. Zhou, *Curr. Appl. Phys.* **2011**, *11*(3), 551–554.
[25] H. LI, S. Zhang, S. Zhou, X. Cao, Y.. Zheng, *J. Phys. Chem. C.* **2009**, *113*(30), 13115–13120.
[26] S. Hu, H. Zhou, X. Zhou, X. Luan, K. Wang, X. Chen, *Ceram. Int.* **2020**, *46*(15), 24552–24556.
[27] K. Kishida, T. Watanabe, *J. Phys. Chem. Solids.* **2014**, *75*(4), 486–490.
[28] A. H. Reshak, Z. A. Alahmed, J. Bila, V. V. Atuchin, B. G. Bazarov, O. D. Chimitova, M. S. Molokeev, I. P. Prosvirin, A. P. Yelisseyev, *J. Phys. Chem. C.* **2016**, *120*(19), 10559–10568.
[29] V. V. Atuchin, A. S. Aleksandrovsky, O. D. Chimitova, T. A. Gavrilova, A. S. Krylov, M. S. Molokeev, A. S. Oreshonkov, B. G. Bazarov, J. G. Bazarova *J. Phys. Chem. C.* **2014**, *118*(28), 15404–15411.
[30] I. M. Shmyt'ko, E. A. Kudrenko, V. V. Sinitsyn, B. S. Red'kin, E. G. Ponyatovsky, *JETP Lett.* **2005**, *82*, 409–412.
[31] D. Machon, V. P. Dmitriev, V. V. Sinitsyn, G. Lucazeau, *Phys. Rev. B.* **2004**, *70*(9), 094117.
[32] C. A. Kodaira, H. F. Brito, O. L. Malta, O. A. Serra, *J. Lumin.* **2003**, *101*(1–2), 11–21.
[33] H. B. Lal, N. Dar, *Physica B + C.* **1976**, *84*(2), 254–258.
[34] M. Rahimi-Nasrabadi, S. M. Pourmortazavi, M. R. Ganjali, A. R. Banan, F. Ahmadi, *J. Mol. Struct* **2014**, *1074*, 85–91.
[35] H. B. Lal, N. Dar, L. Lundgren, *J. Phys. Soc. Jpn.* **1976**, *41*(4), 1216–1223.
[36] F. Lahoz, N. P. Sabalisck, E. Cerdeiras, L. Mestres, *J. Alloys Compd.* **2015**, *649*, 1253–1259.
[37] K. H. Cho, K. P. Hong, S. Nahm, B. Y. Jang, J. S. Park, S. J. Yoo, *Electroceram.* **2009**, *22*, 98–104.
[38] C. Qin, Y. Huang, G. Chen, L. Shi, X. Qiao, J. Gan, H. J. Seo, *Mater. Lett.* **2009**, *63*(13-14), 1162–1164.
[39] M. U. Abulkhaev, M. S. Molokeev, A. S. Oreshonkov, A. S. Aleksandrovsky, A. V. Kertman, D. N. Kamaev, O. V. Trofimova, A. V. Elyshev, O. V. Andreev, *J. Solid State Chem.* **2023**, *322*, 123991.
[40] V. M. Grigorchenko, M. S. Molokeev, A. S. Oreshonkov, A. S. Aleksandrovsky, A. V. Kertman, M. U. Abulkhaev, A. S. Mereshchenko, I. O. Yurev, N.A. Shulaev, D. N. Kamaev, A. V. Elyshev, O. V. Andreev, *J. Solid State Chem.* **2024**, *333*, 124640.
[41] J. A. Alonso, F. Rivillas, M. J. Martınez-Lope, V. Pomjakushin, *J. Solid State Chem.* **2004**, *177*(7), 2470–2476.

[42] S. V. Borisov, R. F. Klevtsova, *Kristallografiya.* **1970**, *15*(1), 38–42.
[43] A. A. Coelho, *J. Appl. Crystallogr.* **2018**, *51*(1), 210–218.
[44] P. S. Dutta, A. Khanna, *ECS J. Solid State Sci. Technol.* **2013**, *2*(2), 3153–3167.
[45] M. G. Nikolić, D. J. Jovanović, M. D. Dramićanin, *Appl. Opt.* **2013**, *52* (8), 1716–1724.
[46] S. Zhou, C. Duan, S. Han, *Dalton Trans.* **2018**,*47*, 1599–1603.
[47] R. L. Blaine, H. E. Kissinger, *Thermochim. Acta.* **2012**, *540*, 1–6.
[48] J. Llopiz, M. M. Romero, A. Jerez, Y. Laureiro, *Thermochim. Acta.* **1995**, *256*, 205–211.
[49] T. Ozawa, *Bull. Chem. Soc. Jpn.* **1965**, *38*(11),1881–1886.
[50] C. D. Doyle, *J. Appl. Polym. Sci.* **1961**, *15*, 285–292.
[51] S. J. Clark, M. D. Segall, C. J. Pickard, P. J. Hasnip, M. I. J. Probert, K. Refson, M. C. Payne, *Z. Kristallogr., Cryst. mater.* **2005**, *220*(5-6), 567–570.
[52] S. L. Dudarev, G. A. Botton, S. Y. Savrasov, C. J. Humphreys, A. P. Sutton, *Phys. Rev. B.* **1998**, *57* (3), 1505–1509.
[53] A. P. Bartók, J. R. Yates, *J. Chem. Phys.* **2019**, *150*, 161101.
[54] J. Sun, R. C. Remsing, Y. Zhang, Z. Sun, A. Ruzsinszky, H. Peng, Z. Yang, A. Paul, U. Waghmare, W. Xifan, M. L. Klein, J. P. Perdew, *Nat. Chem.* **2016**, *8*, 831–836.
[55] A. H. Reshak, Z. A. Alahmed, J. Bila, V. V. Atuchin, B. G. Bazarov, O. D. Chimitova, M. S. Molokeev, I. P. Prosvirin, A. P. Yelisseyev, *J. Phys. Chem. C.* **2016**, *120*(19), 10559–10568.
[56] A. S. Oreshonkov, E. M. Roginskii, V. V. Atuchin, *J. Phys. Chem. Solids.* **2020**, *137*, 109219.

Manuscript received: May 29, 2024
Accepted manuscript online: July 8, 2024
Version of record online: ■■, ■■

RESEARCH ARTICLE

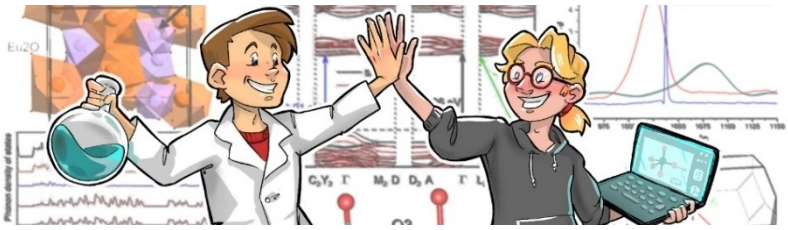

Complex oxides Eu_2MeO_6 (Me–Mo, W), $Eu_2W_2O_9$ were obtained by a solid-phase reaction between binary oxides. The thermodynamic and kinetic mechanisms of the reaction processes were established using a variety of physical-chemical methods. Calculations of absorption spectra are shown to be superior to band structure analysis in the determination of optical band gaps. In this work, the experimental data are in good agreement with the theoretical models.

*Y. V. Seredina, A. S. Oreshonkov, M. S. Molokeev, A. E. Sedykh, A. S. Aleksandrovsky, M. A. Zhernakov, N. A. Khritokhin, N. O. Azarapin, P. O. Glukhova, N. A. Shelpakova, K. Müller-Buschbaum, Y. G. Denisenko**